INTERNATIONAL JOURNAL FOR NUMERICAL METHODS IN FLUIDS
Int. J. Numer. Meth. Fluids 2000; **32**: 545–567

Numerical study of vortex shedding from a rotating cylinder immersed in a uniform flow field

Mo-Hong Chou*

Institute of Mathematics, Academia Sinica, Nankang, Taipei, 11529 Taiwan, Republic of China

SUMMARY

A numerical study is made of the unsteady two-dimensional, incompressible flow past an impulsively started translating and rotating circular cylinder. The Reynolds number (Re) and the rotating-to-translating speed ratio (α) are two controlled parameters, and the influence of their different combinations on vortex shedding from the cylinder is investigated by the numerical scheme sketched below. Associated with the streamfunction (ψ)–vorticity (ω) formulation of the Navier–Stokes equations, the Poisson equation for ψ is solved by a Fourier/finite-analytic, separation of variable approach. This approach allows one to attenuate the artificial far-field boundary, and also yields a global conditioning on the wall vorticity in response to the no-slip condition. As for the vorticity transport equation, spatial discretization is done by means of finite difference in which the convection terms are handled with the aid of an ENO (essentially non-oscillatory)-like data reconstruction process. Finally, the interior vorticity is updated by an explicit, second-order Runge–Kutta method. Present computations fall into two categories. One with $Re = 10^3$ and $\alpha \leq 3$; the other with $Re = 10^4$ and $\alpha \leq 2$. Comparisons with other numerical or physical experiments are included. Copyright © 2000 John Wiley & Sons, Ltd.

KEY WORDS: finite difference; finite analytic; essentially non-oscillatory; upwinding; vorticity conditioning; explicit time marching; rotating cylinder

1. INTRODUCTION

Unsteady flow past an impulsively started circular cylinder has long been of interest both experimentally and theoretically. There are two relevant parameters in such a study. Namely, the Reynolds number (Re) and the rotating-to-translating speed ratio (α). Although the geometry is simple, different combinations of Re and α have already made the flow patterns near the cylinder complicated enough to represent many phenomena in fluid dynamics. Early developments on this subject are described in classic works such as Prandtl

* Correspondence to: Institute of Mathematics, Academia Sinica, Nankang, Taipei, Taiwan 11529, Republic of China.
E-mail: chou@math.sinica.edu.tw

CCC 0271–2091/2000/050545–23$17.50

Received September 1996
Revised February 1999

and Tietjens [1] and Batchelor [2]. Recent experimental studies can be found in the works of Taneda [3], Bouard and Contanceau [4] and Coutanceau and Ménard [5].

With the advance in computer power, numerical simulation has become a cost-effective alternative to physical experiment. Such a situation has been demonstrated by many researchers. Close agreement with experiment in the initial developments of a flow can be achieved with well-designed schemes, as shown by Badr and Dennis [6], Loc and Bouard [7], and Badr *et al.* [8]. However, the vast variety among the existing numerical schemes implies that there are certain limitations for each individual scheme. Therefore, it still leaves much room for algorithm design.

From the previous numerical studies of flow past a translating and rotating cylinder we notice, among others, two types of methodologies. Badr and Dennis [6] employed a high-order-accurate Fourier method which contained a delicate treatment about the no-slip condition as well as the initial flow condition. A form of Crank–Nicolson procedure was used for time-marching. Chang and Chern [9], on the other hand, employed a deterministic, hybrid vortex method which contained a semi-Lagrangian feature suitable for high-Reynolds number flow. The time-marching was based on a midpoint rule. It is then of great interest to develop a finite difference-flavored scheme bearing a similar performance.

In this work we present such a scheme, whose features are sketched as follows. Associated with the streamfunction (ψ)–vorticity (ω) formulation of the Navier–Stokes equations, the Poisson equation for ψ is solved by a Fourier/finite-analytic, separation of variable approach. This approach allows one to attenuate the artificial far-field boundary, and also yields a global conditioning on the wall vorticity in response to the no-slip condition. As for the vorticity transport equation, spatial discretization is done by means of finite difference in which the convection terms are handled with the aid of an ENO (essentially non-oscillatory)-like data reconstruction process. Finally, the interior vorticity is updated by an explicit, second-order Runge–Kutta method. These features are detailed in Sections 2 and 3. We note in passing that a scheme which performs well for flow past a stationary cylinder is likely to become inadequate for flow past a cylinder rotating at a significant speed.

One primary advantage of numerical simulation is the support of detailed flow patterns in the near wake. Such patterns can offer a topological analysis, which is crucial to understand the mechanism of vortex shedding. Another advantage is the detailed time history of certain quantities such as drag and lift coefficients, which also reflect the behavior of vortex shedding. Present computations fall into two categories. One with $Re = 10^3$ and $\alpha \leq 3$; the other with $Re = 10^4$ and $\alpha \leq 2$. The computed results are reported in Section 4, in which comparisons with other numerical or experimental results are included.

2. PROBLEM FORMULATION

Consider a uniform incompressible flow, with velocity $(U_\infty, 0)$ at infinity, past a circular cylinder rotating counterclockwise at a constant speed α relative to U_∞ The flow is governed

by the Navier–Stokes equations which, after non-dimensionalization, are written in terms of vorticity (ω) and streamfunction (ψ) as follows.

$$\omega_t + \psi_y \omega_x - \psi_x \omega_y = \frac{2}{Re}(\omega_{xx} + \omega_{yy}); \tag{1}$$

$$\psi_{xx} + \psi_{yy} = -\omega; \tag{2}$$

$$\psi = 0 \text{ and } x\psi_x + y\psi_y = -\alpha \text{ on cylinder's boundary, for } t > 0; \tag{3}$$

$$(\psi_x, \psi_y) \to (0, 1) \text{ as } x^2 + y^2 \to \infty; \tag{4}$$

$$\psi(x, y, t = 0) = \psi^\circ(x, y) \equiv \text{ potential flow.} \tag{5}$$

In Equations (1)–(5) the underlying length scale is $D/2$ where D denotes the diameter of a cylinder, while the Reynolds number Re is defined as $Re = DU_\infty/v$, where v stands for the kinematic viscosity.

It has been shown that a generally feasible approach to solve Equations (1)–(5) is direct numerical simulation. To facilitate the associated computations, we introduce a stretched polar co-ordinate system, after Smith and Stansby [10].

$$x + iy = \exp(\eta + i(\pi - \xi)), \quad 0 \le \xi \le 2\pi \quad \text{and} \quad \eta \ge 0; \tag{6}$$

$$\eta = \log(1 + B(\exp(Aj) - 1)), \quad j = 0, 1, \ldots, N. \tag{7}$$

In Equation (7) N is a prescribed positive integer, and the parameters A and B are chosen such that $BA = \mathcal{O}(1/\sqrt{Re})$ and $1 + B(\exp(AN) - 1) = r_\infty$. Here we assume the vorticity is essentially bounded within a large circle of radius r_∞ and center $(0, 0)$, throughout the whole computation.

By virtue of Equation (6) the Navier–Stokes equations (Equations (1)–(4)) are converted into the following:

$$J\omega_t + \psi_\eta \omega_\xi - \psi_\xi \omega_\eta = \frac{2}{Re}(\omega_{\xi\xi} + \omega_{\eta\eta}), \tag{8}$$

$$\psi_{\xi\xi} + \psi_{\eta\eta} = -J\omega, \text{ where } J = \exp(2\eta); \tag{9}$$

$$\partial\psi/\partial\eta = -\alpha \text{ and } \psi = 0 \text{ on } \eta = 0, \tag{10}$$

$$\partial(\psi - \psi^\circ)/\partial\eta \to 0 \text{ as } \eta \to \infty, \tag{11}$$

where $\psi^\circ = (\exp(\eta) - \exp(-\eta)) \sin \xi$.

3. THE NUMERICAL METHOD

First, the transformed Poisson equation (Equation (9)) together with the boundary conditions (Equations (10) and (11)) are dealt with by a Fourier/finite-analytic separation of variable approach. Assume ψ and ω have the following forms of Fourier expansion at any instant:

$$\psi = \psi^\circ + \sum_k (f_k(\eta) \cos k\xi + g_k(\eta) \sin k\xi), \tag{12}$$

$$\omega = \sum_k (p_k(\eta) \cos k\xi + q_k(\eta) \sin k\xi). \tag{13}$$

Then, for each k, we have the following two-point boundary value problems (BVPs) associated with f_k and g_k:

$$f_k'' - k^2 f_k = -Jp_k, \tag{14}$$

$$f_k(0) = f_k'(\infty) = 0, \text{ and } f_k'(0) = -\alpha\delta_k^0; \tag{15}$$

$$g_k'' - k^2 g_k = -Jq_k, \tag{16}$$

$$g_k(0) = g_k'(\infty) = 0, \text{ and } g_k'(0) = -2\delta_k^1; \tag{17}$$

$$\text{where } \delta_k^j = 1 \text{ if } j = k, \text{ and } = 0 \text{ otherwise} \tag{18}$$

Analytic solutions to these problems are pursued. However, the Fourier coefficients, $p_k(\eta)$ and $q_k(\eta)$, for ω were known numerically (e.g., by fast Fourier transform) only for those discrete η_j values determined by Equation (7). Denote these discrete data by $p_{k,j}$ and $q_{k,j}$. A continuous version is constructed in this work by piecewise linear interpolation over $p_{k,j}$ and $q_{k,j}$ respectively. Owing to such a low-order approximation, we shall call the resultant approach finite-analytic.

The desire for analytic solutions to the BVPs, (Equations (14) and (15)) and (Equations (16) and (17)), is evoked by two considerations. Firstly, these problems are over a semi-infinite domain. Secondly, there are overspecified, no-slip boundary conditions around the cylinder. We thus need an appropriate treatment for Neumann conditions occurring both at infinity and at the cylinder's boundary.

Let $[0, \infty) = \cup_{j=1}^{N-1}[\eta_{j-1}, \eta_{j+1}] \cup [\eta_{N-1}, \infty)$. We partition the problem (Equations (14) and (15)) accordingly into a system of mutually-coupled subproblems:

$$f_k'' - k^2 f_k = -Jp_k \text{ for } \eta \in [\eta_{j-1}, \eta_{j+1}] \text{ and} \tag{19}$$

$$f_k(\eta_{j-1}) = f_{k,j-1}, f_k(\eta_{j+1}) = f_{k,j+1}, 1 \le j \le N-1; \tag{20}$$

(the condition $f'_k(0) = -\alpha\,\delta^0_k$ will be addressed later)

$$f''_k - k^2 f_k = 0 \text{ for } \eta \in [\eta_{N-1}, \infty] \text{ and} \tag{21}$$

$$f_k(\eta_{N-1}) = f_{k,N-1}, f'_k(\infty) = 0. \tag{22}$$

The right-hand side of Equation (21) is zero since the vorticity ω is generated from the cylinder's boundary, and is plausible to be zero in the far wake (i.e., $p_{k,j} = 0$ for $j \geq N-1$) within a finite period of evolution. Note that the problem (Equations (16) and (17)) can be handled likewise, and will be skipped in the sequel.

Problems (19)–(22) can be solved analytically with the aid of the Green function. It gives a system of three-point relations among the unknowns $f_{k,j}$ in which the j-th entry is expressed as follows. Let $a = \eta_j - \eta_{j-1}$, $b = \eta_{j+1} - \eta_j$, and

$$G_k(y) = \frac{\exp(2(\eta_j + y))}{k \sinh(k(a+b))} \cdot \begin{cases} \sinh(kb)\sinh(k(a+y)) \text{ if } -a \leq y \leq 0 \\ \sinh(ka)\sinh(k(b-y)) \text{ if } 0 \leq y \leq b. \end{cases} \tag{23}$$

Then, for $1 \leq j \leq N-1$, we have

$$-\gamma f_{k,j-1} + f_{k,j} - \delta f_{k,j+1} = \Gamma p_{k,j-1} + \Theta p_{k,j} + \Delta p_{k,j+1} \tag{24}$$

where

$$\gamma = \sinh(kb)/\sinh(k(a+b)),\ \delta = \sinh(ka)/\sinh(k(a+b)), \tag{25}$$

and

$$\Gamma = -\int_{-a}^{0} (y/a) G_k(y)\,\mathrm{d}y,\ \Delta = \int_{0}^{b} (y/b) G_k(y)\,\mathrm{d}y,\ \Theta = \int_{-a}^{b} G_k(y)\,\mathrm{d}y - \Gamma - \Delta. \tag{26}$$

For $j = N$, the relation is reduced to

$$-\gamma f_{k,N-1} + f_{k,N} = 0, \text{ where } \gamma = \exp(-ka). \tag{27}$$

Once this system of equations has been solved for $f_{k,j}$, the corresponding first derivatives $f'_{k,j}$ are also available analytically. Here we replace G_k by H_k as

$$H_k(y) = \frac{\exp(2(\eta_j + y))}{\sinh(k(a+b))} \cdot \begin{cases} -\cosh(kb)\sinh(k(a+y)) \text{ if } -a \leq y \leq 0 \\ \cosh(ka)\sinh(k(b-y)) \text{ if } 0 \leq y \leq b. \end{cases} \tag{28}$$

Then, for $1 \leq j \leq N-1$,

$$f'_{k,j} = -\gamma' f_{k,j-1} + \delta' f_{k,j+1} + \Gamma' p_{k,j-1} + \Theta' p_{k,j} + \Delta' p_{k,j+1} \tag{29}$$

where

$$\gamma' = k \cosh(kb)/\sinh(k(a+b)),\ \delta' = k \cosh(ka)/\sinh(k(a+b)), \tag{30}$$

and

$$\Gamma' = -\int_{-a}^{0} (y/a) H_k(y)\, \mathrm{d}y,\ \Delta' = \int_{0}^{b} (y/b) H_k(y)\, \mathrm{d}y,\ \Theta' = \int_{-a}^{b} H_k(y)\, \mathrm{d}y - \Gamma' - \Delta'. \tag{31}$$

Again, for $j = N$, the relation is reduced to

$$f'_{k,N} = -\gamma' f_{k,N-1}, \text{ where } \gamma' = k \exp(-ka). \tag{32}$$

To handle the no-slip condition, the derivative at $\eta = 0$ is obtained by the same token:

$$f'_{k,0} = -\gamma_0 f_{k,0} + \delta_0 f_{k,1} + \Theta_0 p_{k,0} + \Delta_0 p_{k,1} \tag{33}$$

where

$$\gamma_0 = k \coth(kb),\ \delta_0 = k/\sinh(kb),\ b = \eta_1, \tag{34}$$

and

$$\Delta_0 = \int_{0}^{b} (y/b) S_k(y)\, \mathrm{d}y,\ \Theta_0 = \int_{0}^{b} S_k(y)\, \mathrm{d}y - \Delta_0,\ S_k(y) = \exp(2y) \sinh(k(b-y))/\sinh(kb). \tag{35}$$

Let us check the contribution to Equation (33) by each individual $p_{k,j}$. To this end, set $p_{k,j} = p^{\ell}_{k,j} = \delta^{\ell}_{j}$ to construct a tent-like p_k in Equation (14), and repeat the whole process from Equation (14) through Equation (35) for $0 \leq \ell \leq N-1$. Denote the thus obtained component of $f'_{k,0}$ by $\lambda_{k,\ell}$. Then Equation (33) can be rewritten as

$$f'_{k,0} = \sum_{\ell=0}^{N-1} \lambda_{k,\ell} p_{k,\ell}. \tag{36}$$

Since $f'_{k,0}$ are given *a priori*, as shown in Equation (15), and $p_{k,j}$ with $j > 0$ are in general governed by the vorticity transport equation (Equation (8)), the expression (Equation (36)) therefore provides a means to determine the Fourier coefficients of the wall vorticity:

$$p_{k,0} = \left(f'_{k,0} - \sum_{\ell=0}^{N-1} \lambda_{k,\ell} p_{k,\ell} \right) \Big/ \lambda_{k,0}. \tag{37}$$

Such a global conditioning on wall-vorticity is in spirit similar to the projection method employed in our previous works [11–13], but relates more directly to the computation of streamfunction and its derivatives.

For flow at high Reynolds number, the stability of assigning the wall vorticity via Equation (37) might not be adequate when the rotating-to-translating speed ratio, α, is large. Such a situation can be improved if we also allow some *a posteriori* correction on $p_{k,1}$. For example, $p_{k,0}$ and $p_{k,1}$ are determined simultaneously by

$$\lambda_{k,0} p_{k,0} + \lambda_{k,1} p_{k,1} = f'_{k,0} - \sum_{\ell=2}^{N-1} \lambda_{k,\ell} p_{k,\ell}, \tag{38}$$

$$\left(\frac{p_{k,1} - p_{k,0}}{\eta_1 - \eta_0} \right)^2 + \left(\frac{p_{k,2} - p_{k,1}}{\eta_2 - \eta_1} \right)^2 = \text{ minimum.} \tag{39}$$

Such a setting may violate the vorticity transport equation along the first grid line immediately next to the cylinder. By comparing with other numerical experiments, we shall show in the next section the violation is minor, however.

Let us summarize the numerical method presented thus far. Given ω at a certain time step. (i) Compute its ξ-direction Fourier coefficients $p_{k,j}$ and $q_{k,j}$ at $\eta = \eta_j$ determined by Equation (7); (ii) check the no-slip condition by adjusting the wall values $p_{k,0}$ and $p_{k,1}$ via Equations (38) and (39); (iii) solve for $f_{k,j}$ the tridiagonal linear system formed by Equations (24) and (27); (iv) apply formulas (29) and (32) to determine the derivatives $f'_{k,j}$; (v) obtain $g_{k,j}$ and $g'_{k,j}$ by the same token; and (vi) apply fast Fourier transform to restore ψ, ψ_ξ, and ψ_η via expression (12), and thus complete the solution to Equations (9)–(11).

Here is a further remark on the above procedure. For high-Reynolds-number flow the regularity of ω is limited by the presence of many secondary vortices around the cylinder. In other words, the Fourier coefficients $p_{k,j}$ and $q_{k,j}$ may decay slowly with k, and some sort of filtering is called for. The filter should not only prevent the erratic growth of Fourier modes near the Nyquist bound, but also allow sufficient modes to pass in order to preserve some delicate mutual cancellation. By trial and error, the following exponential filter [14] is adopted.

$$p_{k,j} \leftarrow p_{k,j} \exp(-\sigma(2k/M)^\mu);\ q_{k,j} \leftarrow q_{k,j} \exp(-\sigma(2k/M)^\mu),\ 0 \le k \le M/2; \tag{40}$$

where M is the number of grid points, $\mu = 16$, and $\exp(-\sigma) =$ machine zero.

Next we proceed to discretize the transformed vorticity transport equation (Equation (8)). It starts by rewriting Equation (8) as

$$J\omega_t = \mathscr{H}(\omega) \equiv -\left(\psi_\eta \omega - \frac{2}{Re} \omega_\xi \right)_\xi - \left(-\psi_\xi \omega - \frac{2}{Re} \omega_\eta \right)_\eta. \tag{41}$$

Spatial differentiations on the parenthesized terms are approximated by centered differencing such as $(\cdot)_\xi \doteq 1/\Delta\xi[(\cdot)_{i+1/2,j} - (\cdot)_{i-1/2,j}]$ and $(\cdot)_\eta \doteq 1/\eta'(j)[(\cdot)_{i,j+1/2} - (\cdot)_{i,j-1/2}]$. Similarly, the derivatives of ω within each parenthesis are approximated as $\omega_\xi \doteq 1/\Delta\xi(\omega_{i+1,j} - \omega_{i,j})$ and $\omega_\eta \doteq 1/\eta'(j+1/2)(\omega_{i,j+1} - \omega_{i,j})$.

The midway convective fluxes $(\psi_\eta\omega)_{i+1/2,j}$ and $(-\psi_\xi\omega)_{i,j+1/2}$ are to be evaluated via ENO interpolation as developed by Harten *et al.* [15]. However, there are circumstances showing that the original third-order ENO interpolation is inadequate in shape-preserving in the proximity of the cylinder. An improvement is adapted from Huynh [16], and is briefly described as follows.

Let $\not{p}$ denote the ξ-primitive of $\psi_\eta\omega$, or the η-primitive of $-\psi_\xi\omega$, and we wish to interpolate $\not{p}$ over the interval $[\xi_{i-1/2}, \xi_{i+1/2}]$ using the relevant first-, second-, and third-order divided differences: c_i, $\{d_{i-1/2}, d_{i+1/2}\}$, $\{e_{i-1}, e_i, e_{i+1}\}$. Then, up to the constant of $\not{p}$ at $\xi_{i-1/2}$, we have the following five candidates for Newton interpolation:

$$\not{p}_1 = c_i(\xi - \xi_{i-1/2}), \tag{42}$$

$$\not{p}_{2-} = \not{p}_1 + d_{i-1/2}(\xi - \xi_{i-1/2})(\xi - \xi_{i+1/2}), \tag{43}$$

$$\not{p}_{2+} = \not{p}_1 + d_{i+1/2}(\xi - \xi_{i-1/2})(\xi - \xi_{i+1/2}), \tag{44}$$

$$\not{p}_{3-} = \not{p}_{2-} + \langle e_{i-1}, e_i, 0\rangle(\xi - \xi_{i-3/2})(\xi - \xi_{i-1/2})(\xi - \xi_{i+1/2}), \tag{45}$$

$$\not{p}_{3+} = \not{p}_{2+} + \langle e_i, e_{i+1}, 0\rangle(\xi - \xi_{i-1/2})(\xi - \xi_{i+1/2})(\xi - \xi_{i+3/2}), \tag{46}$$

where $\langle a, b, c\rangle$ means the median item among the collection of a, b, c. (e.g., $\langle a, b, c\rangle = a$ if $b \le a \le c$ or $c \le a \le b$).

Based on these multi-order, polynomial interpolations, (Equations (42)–(46)), the right derivative of $\not{p}$ at $\xi_{i-1/2}$ is defined as

$$\not{p}'^{+}_{i-1/2} = \langle \not{p}'_1, \not{p}'_{3-}, \not{p}'_{3+}\rangle \rfloor_{\xi=\xi_{i-1/2}}. \tag{47}$$

Similarly, the left derivative of $\not{p}$ at $\xi_{i+1/2}$ is defined as

$$\not{p}'^{-}_{i+1/2} = \langle \not{p}'_1, \not{p}'_{3-}, \not{p}'_{3+}\rangle \rfloor_{\xi=\xi_{i+1/2}}. \tag{48}$$

Judging by the upwind direction, either $\not{p}'^{-}_{i+1/2}$ or $\not{p}'^{+}_{i+1/2}$ are issued to give the midway convective flux $(\psi_\eta\omega)_{i-1/2,j}$.

Using $\mathscr{H}(\omega)$ to denote the total effect of convection and diffusion, as shown in Equation (41), the interior vorticity is then updated by an explicit, second-order Runge–Kutta scheme:

$$J\omega^{n+1/2} = J\omega^n + \frac{\Delta t}{2}\mathscr{H}(\omega^n) \tag{49}$$

$$J\omega^* = J\omega^n + \Delta t\,\mathscr{H}(\omega^{n+1/2}) \tag{50}$$

$$J\omega^{n+1} = J\omega^n + \frac{\Delta t}{6}[\mathscr{H}(\omega^n) + 4\mathscr{H}(\omega^{n+1/2}) + \mathscr{H}(\omega^*)] \tag{51}$$

Although a third-order-accurate Runge–Kutta scheme can be achieved by the same amount of arithmetic operations (see [17] for example), we find the proposed one is more robust by examining their respective stability region.

During the numerical simulation an important output is the fluid dynamic quantities such as drag and lift. For high-Reynolds-number flow the essential part of each quantity is due to the surface pressure. We calculate it with the following theorem developed in our previous works [11–13].

Theorem 1 *Let* $\Omega = \{(x, y) | 1 \le x^2 + y^2 \le 1 + \varepsilon\}$, *and* $\partial\Omega = B_0 \cup B_1$ *where* B_0 *denotes the cylinder's surface. Then, in terms of* ω *and* ψ, *the drag and lift exerted by the non-dimensional surface pressure can be expressed as*

$$\frac{\mathrm{d}}{\mathrm{d}t}\oint_{B_1}\psi\frac{\partial\varphi}{\partial v} + \int_\Omega \omega\frac{\partial(\psi,\varphi)}{\partial(x,y)}\,\mathrm{d}x\,\mathrm{d}y + \frac{2}{Re}\left[\oint_{B_1}\omega\frac{\partial\varphi}{\partial v} - \oint_{B_0}\omega\frac{\partial\varphi}{\partial v}\right]. \tag{52}$$

In terms of polar co-ordinates (*Equation* (6)), *the auxiliary function* φ, *in Equation* (52) *is given by*

$$\varphi = -\frac{\sinh(\eta_\varepsilon - \eta)}{\sinh\eta_\varepsilon}\cdot\begin{cases}\sin\xi \textit{ for drag}\\ \cos\xi \textit{ for lift}\end{cases} \tag{53}$$

where $\eta_\xi = \log(1+\varepsilon)$, *and* ε *is chosen such that* Ω *covers the strongly varied, near-wake vorticity field.*

The skin-friction part of these quantities is handled as usual:

$$(\text{drag, lift})_S = \frac{2}{Re}\oint_{B_0}\omega(\mathrm{d}x, \mathrm{d}y). \tag{54}$$

Note that the closed integral is done counterclockwise. These formulas yield the drag and lift coefficients, C_D and C_L, after being non-dimensionalized by $\rho U_\infty^2 D/2$ where (ρ, U_∞, D) stand for the fluid density, flow speed at infinity, and the cylinder's diameter respectively. The long-term history of these coefficients can be used to estimate of vortex-shedding frequency, if it occurs. The Strouhal number, St, is defined as

$$St = \text{shedding frequency} \cdot D/U_\infty, \tag{55}$$

For initial flow simulation, the following asymptotic result adapted from Badr and Dennis [6] is used to compare with our numerical results.

$$C_D \sim 4\sqrt{2\pi/Rt} + 2\pi/Re; \tag{56}$$

$$C_L \sim -\pi\alpha\lambda(1.2104 + 0.6961\lambda),\ \lambda = 2\sqrt{2t/Re}. \tag{57}$$

Note that the drag formula (Equation (56)) is independent of α, so t should be small enough.

4. WORKED EXAMPLES AND DISCUSSIONS

The numerical performance of our algorithm, as presented in the preceding section, is reported here. The flow situations fall into two categories. One with $Re = 10^3$ and $\alpha \leq 3$; the other with $Re = 10^4$ and $\alpha \leq 2$. The first category has been fairly studied by Badr *et al.* [8], while certain information can be drawn form Chang and Chern [9] for the second category. Thus, the computations serve as a performance test of our method on one hand, and will also provide certain supplementary remarks to the existing observations on the other. We refer readers interested in α varying with time to the companion work [18]. By virtue of Equations (6) and (7), the computational $(\xi \times \eta)$ domain is covered by a 128×80 grid, where $r_\infty = 22$. The explicit time-marching scheme (Equations (49)–(51)) starts with $\Delta t = 0.001$, and escalates into $\Delta t = 0.01$ within the first 20 steps.

We begin with flows at $Re = 10^3$ and $\alpha \leq 3$. The first common point of interest in such a study is the detailed flow pattern in the near wake. Topological analysis such as locating the set of interior stagnation points is crucial in order to understand the mechanism of vortex shedding. This set consists of a front stagnation point and pairs of vortex centers and closure points. Careful (interactive) streamline plots can reveal the existence of such points up to the resolution of the underlying numerical scheme. They are denoted by heavy dots in the figures below. The angular direction of the front stagnation point is denoted in addition by a small filled circle inside the cylinder. The locations of these points are found in good agreement with the above-mentioned references. Their significance in vortex shedding is accounted for via the following sample plots which, for simplicity, are prepared at fixed times: $t = 2$, 3, 4, 6, 7, and 11, for any case of (Re, α).

Figure 1(a) shows an asymmetric pair of vortices (or eddies) formed in rear of the cylinder at $t = 2$ for $\alpha = 0.5$. In what follows we shall call this first upper main vortex E_1 and the first lower one E_2. In contrast to the stationary case, E_1 and E_2 no longer share a downstream closure point. The rotation now favors the growth of E_1, and makes its closure point stay downstream. Meanwhile, the somewhat retarded E_2 turns its closure point toward the cylinder.

Figure 1(b,c) show that E_1 and E_2 each still give birth subsequently to a pair of adjacent secondary vortices. These secondary vortices will be called E_1', E_1'', and E_2', E_2'', accordingly. In these notations a single prime is used if their respective senses of rotation are equal to the adjacent main vortex, and a double prime otherwise. There exists another difference from the

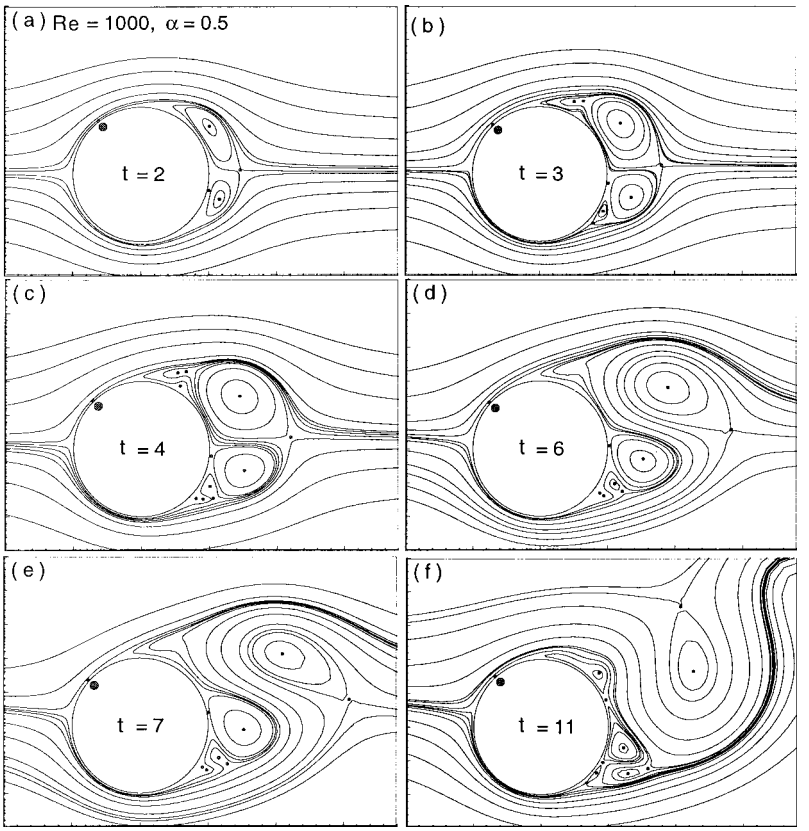

Figure 1. Near-wake flow pattern; (a)–(f) streamline plots.

case of $\alpha = 0$ that a transposition between the closure points of E_2' and E_2'' happens at $t < 4$ for $\alpha = 0.5$.

Figure 1(d) shows that E_1 reaches its maximum at $t \sim 6$, and starts to move downstream. Meanwhile, E_1' and E_1'' decay into bulges. Although the forms of E_1' and E_2'' change little, the adjustment of E_2 along the cylinder's rotation direction is clear in Figure 1(d,e). Such a movement is at the outset of the first cycle of vortex shedding as shown in Figure 1(f).

Figure 2(a–c) show, for $\alpha = 1$, the vortex system formed by E_2, E_2', and E_2'' decays with the rotating speed. However, in Figure 2(d,e) we see an intermediate stage in which E_2, E_2', and E_2'' all shrink away, and restore their sizes quickly, together with another nascent vortex E_3' instead of E_1'.

Owing to the transposition between the closure points of E_2 and E_3', E_1 is completely disengaged from the cylinder. Another transposition between the closure points of E_2' and E_2'' as shown in Figure 1(f) triggers the merger of E_2'' and E_3 to form a new main vortex E_3 as shown in Figure 2(f). The phenomena of alternate vortex shedding as depicted in Figures 1 and 2 result from a series of such transpositions.

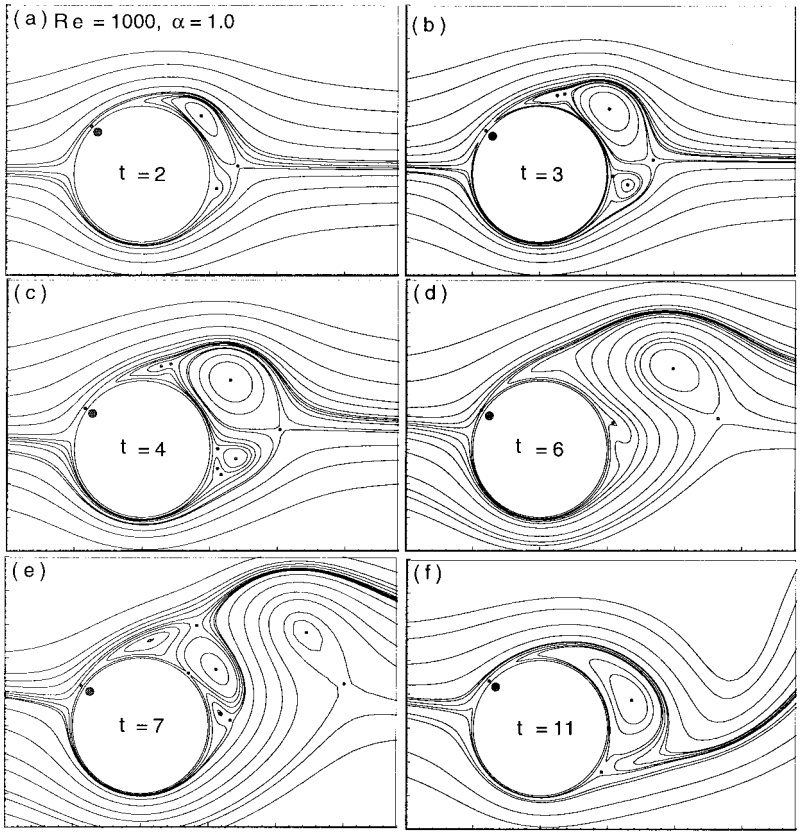

Figure 2. Near-wake flow pattern; (a)–(f) streamline plots.

Figure 3(a–e) show for $\alpha = 2$ that the vortices E_2, E_2' and E_2'' are absent in the early developments of flow. After E_1 is disengaged from the cylinder, a new E_1' appears in such a way that its closure point is transposed with the front stagnation point as shown in Figure 3(f).

Such a peculiarity is also present in the vortex development for $\alpha = 3$. In Figure 4(a–c) the first upper vortex E_1 is now followed by a single secondary vortex E_1'. This E_1', however, receives a better growth condition and causes E_1 to move towards the front stagnation point. Eventually, a transposition between the front stagnation point and the closure point of E_1 takes place, and causes E_1 to be washed out by the incoming flow. The remaining E_1' becomes the main vortex, and sheds away from the cylinder as depicted in Figure 4(d–f). It turns out that a significant layer of fluid next to the cylinder is synchronized to rotate in one direction.

In addition to the above near-wake information, Figure 5(a–c) present an overall vorticity contour at $t = 20$. A regular Bénard–Kármán street can be drawn from Figure 5(a) for $\alpha = 1$. Figure 5(b) shows the formation of such a street is delayed for $\alpha = 2$, while Figure 5(c) shows it is practically suppressed for $\alpha = 3$. These observations are further supported by the time

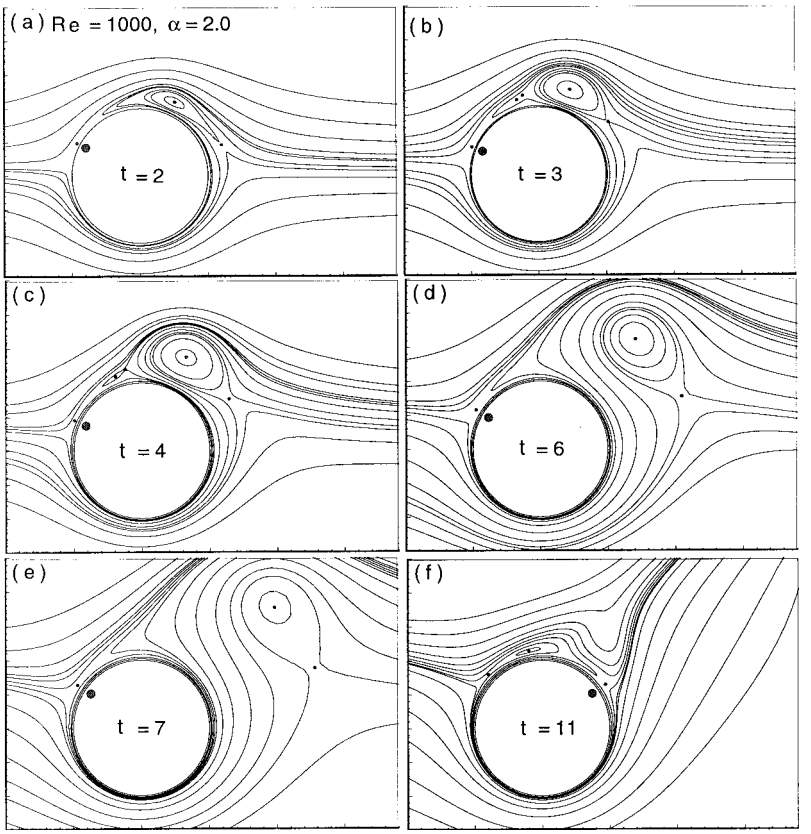

Figure 3. Near-wake flow pattern; (a)–(f) streamline plots.

history of the drag (C_D) and lift (C_L) coefficients. In Figure 6(a,b) the periodic behavior of C_D and C_L is apparent for $\alpha = 0.5$ and 1; while it might be expected for $\alpha = 2$. The predicted Strouhal number (Equation (55)) is about 0.21 for $\alpha \leq 1$, quite similar to the case of $\alpha = 0$.

Figure 7 presents the time history of C_D and C_L for $\alpha = 3$. Although the suppression of vortex shedding can be drawn from their large-time behavior, our computations show a discrepancy from that of Badr *et al.* [8] for $t \geq 5$, beyond which the experimental flow becomes turbulent.

As for the initial behavior of C_D and C_L, Figure 8(a,b) present a comparison with the asymptotic result (Equations (56) and (57)) derived by Badr and Dennis [6] using boundary-layer co-ordinates. In Figure 8(a) we see the present C_D calculation agrees with the asymptotic one before its dependence on α becomes apparent. Figure 8(b) shows that simply setting the initial condition to potential flow yields $C_L \doteq -\alpha$ as $t \to 0$, rather than vanishing into zero by the asymptotic analysis. Apart from this difference, a good agreement is established for small α.

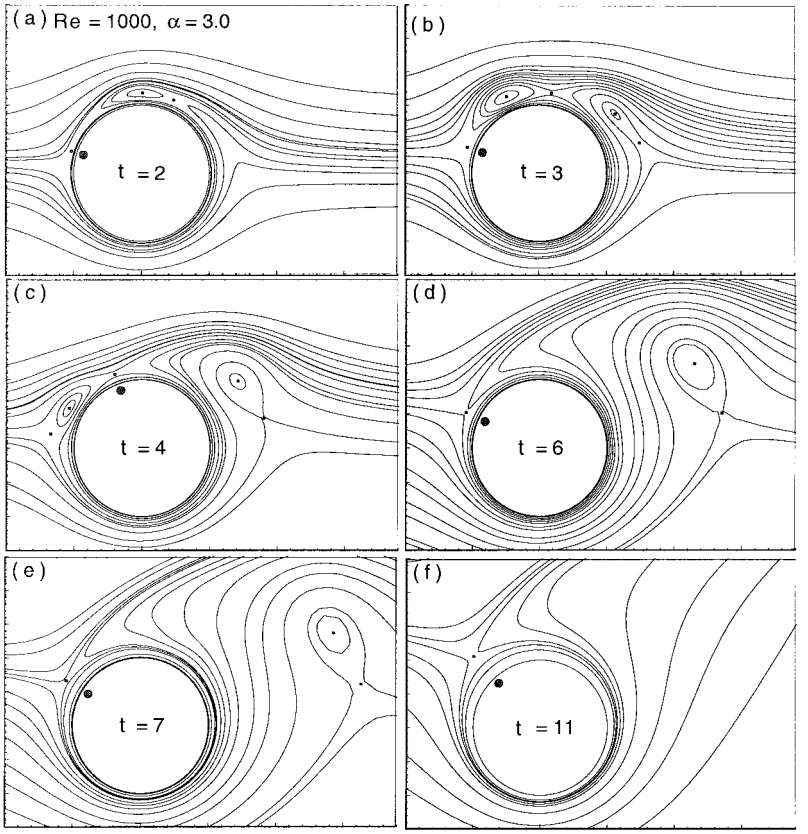

Figure 4. Near-wake flow pattern; (a)–(f) streamline plots.

Yet another comparison for flow with $Re = 10^3$ is given in Figure 9. For $\alpha = 0.5$ and t runs from 1 to 5, the x-component of velocity (u) along the positive x-axis and the positive y-axis are respectively plotted in Figure 9(a,b), together with symbols denoting the experimental results of Badr *et al.* [8].

We now proceed to flows with $Re = 10^4$ and $\alpha \leq 2$. In Figure 10(a) we see the typical β-phenomenon is only preserved by the initial upper vortices, which become E_1, E_1' and E_1'' later as shown in Figure 10(b,c). Again, the upper and lower main vortices, E_1 and E_2, have separate closure points, but in a fashion opposed to the case of $Re = 10^3$. Such a transposition appears to offer E_2 a chance to shed away first from the cylinder. However, it turns out that E_2 is checked by E_1 for a long while for $\alpha = 0.5$, and eventually renders up this chance to E_1 owing to another transposition between their closure points. See Figure 10(d–f).

In Figure 11 we see, for $\alpha = 1$, the second transposition between the closure points of E_1 and E_2 is replaced by the transposition between the closure points of E_1 and E_2'. Therefore, E_2 really sheds away first from the cylinder.

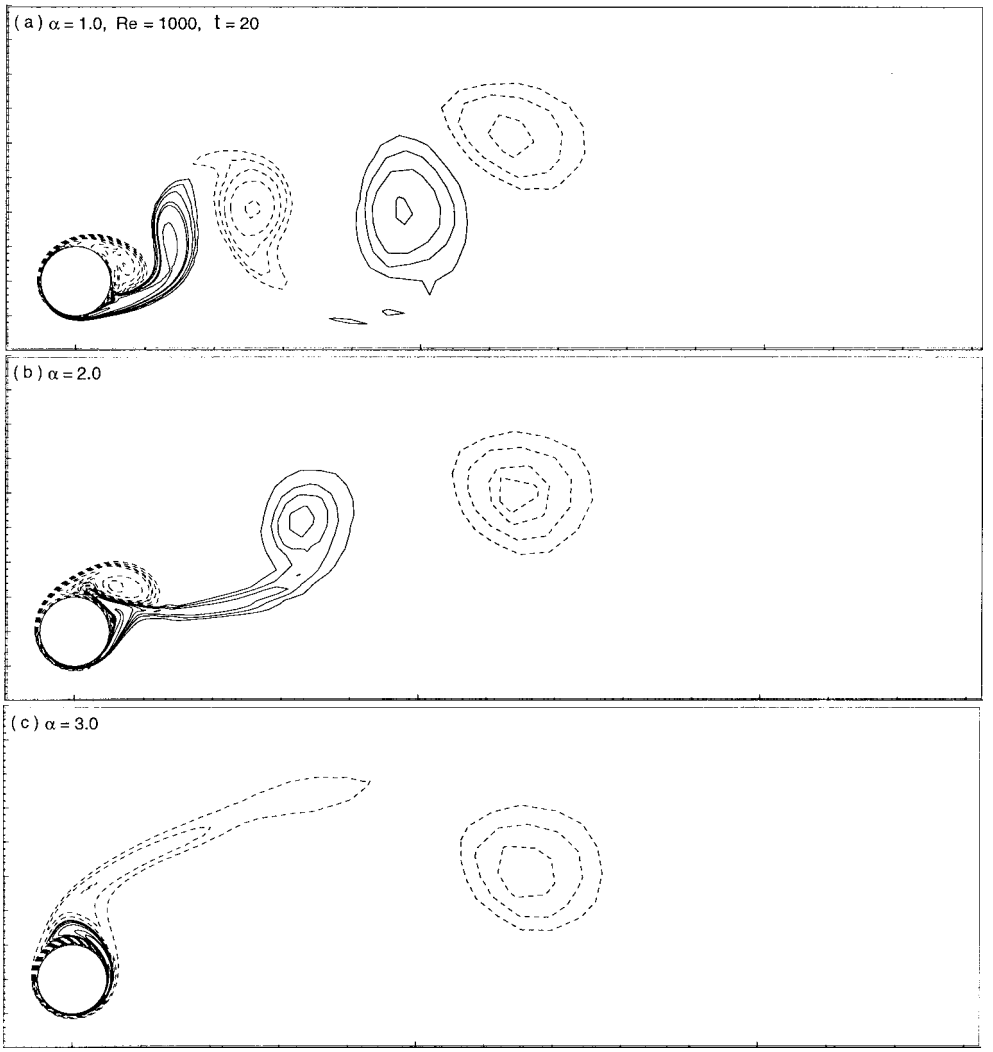

Figure 5. Overall vorticity contours (dash negative).

The scenes shown above seem typical to high-Reynolds-number flow, if α is small. We add here another example with $Re = 2 \times 10^4$, as shown in Figure 12. Whether E_2 succeeds or not in shedding away first, its interaction with E_1 has a significant influence on the lift direction as will be seen below.

Figures 13 and 14 show the flow patterns for $\alpha = 1.5$ and 2 respectively. Apart from the β-phenomenon presented by the upper vortices, and the aforementioned first transposition

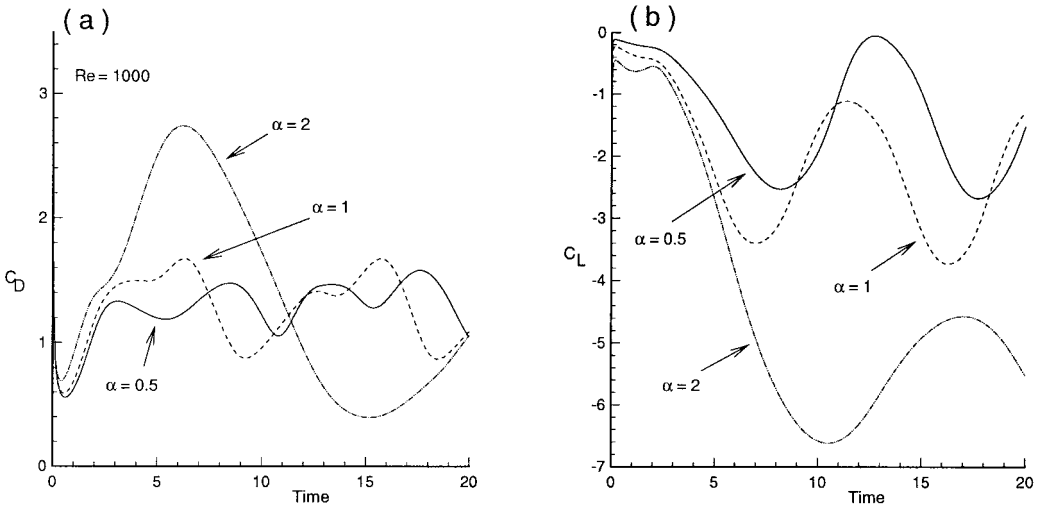

Figure 6. Time histories. (a) Drag coefficient; (b) lift coefficient.

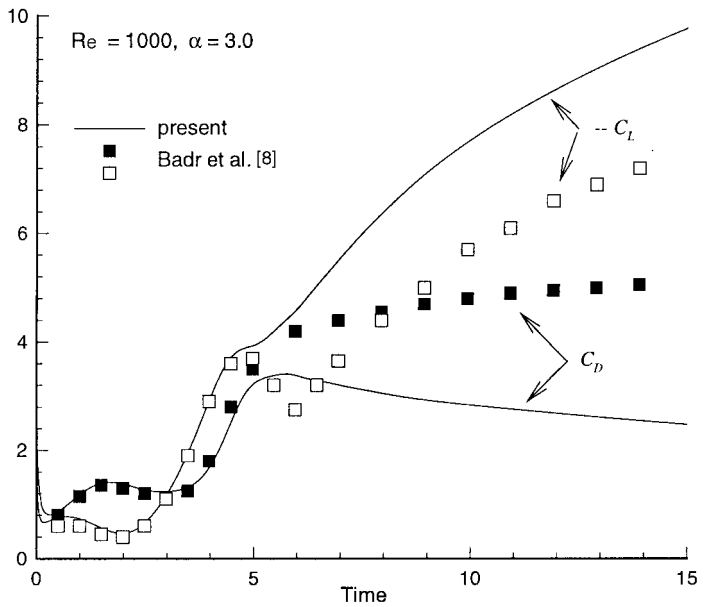

Figure 7. Time histories of drag and lift coefficients. —: present; symbols: reference [8].

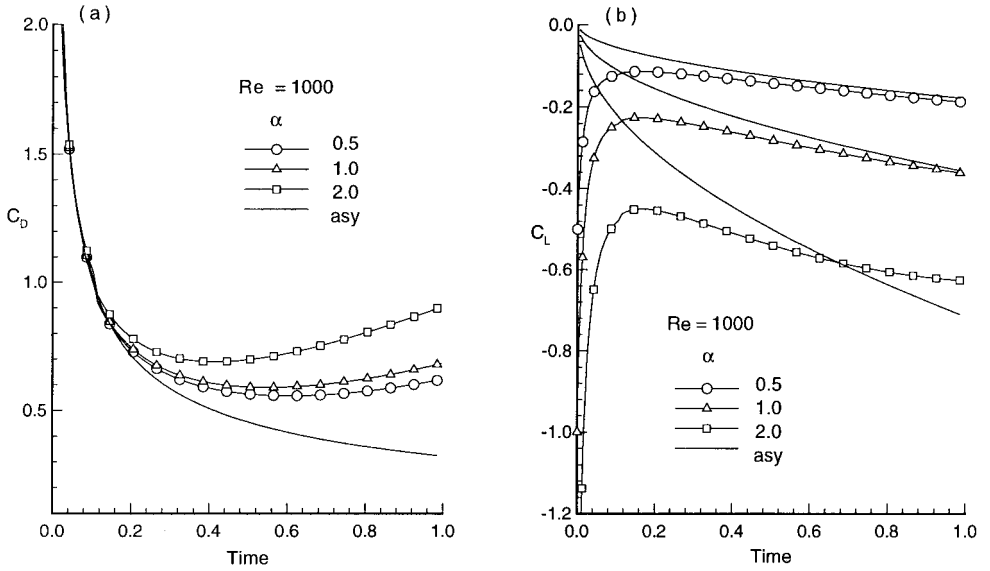

Figure 8. Initial time histories. (a) Drag coefficient; (b) lift coefficient.—: asymptotic result from reference [6].

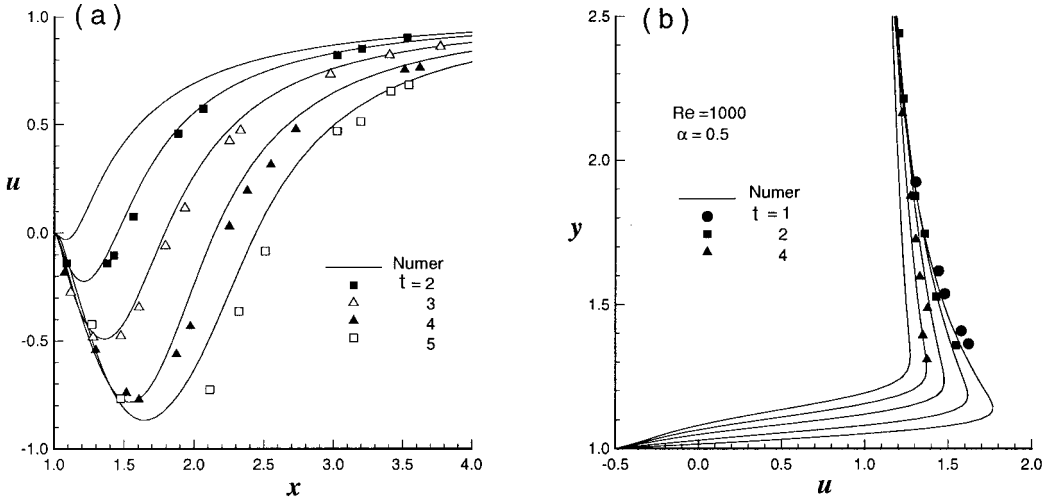

Figure 9. Distribution of x-component velocity (u). (a) Along the positive x-axis; (b) along the positive y-axis. —: present; symbols: experimental results from reference [8].

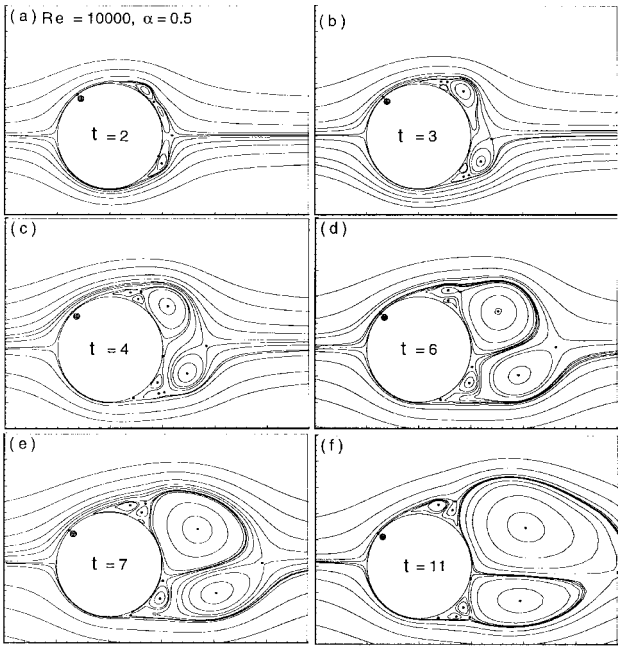

Figure 10. Near-wake flow pattern; (a)–(f) streamline plots.

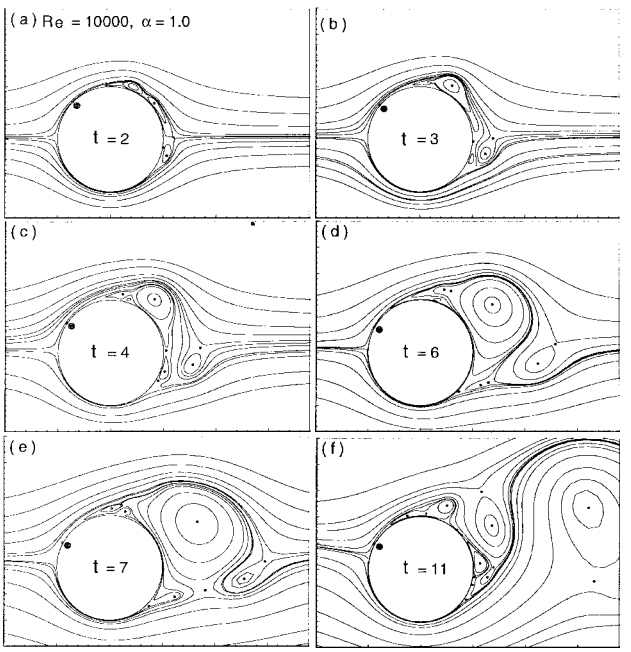

Figure 11. Near-wake flow pattern; (a)–(f) streamline plots.

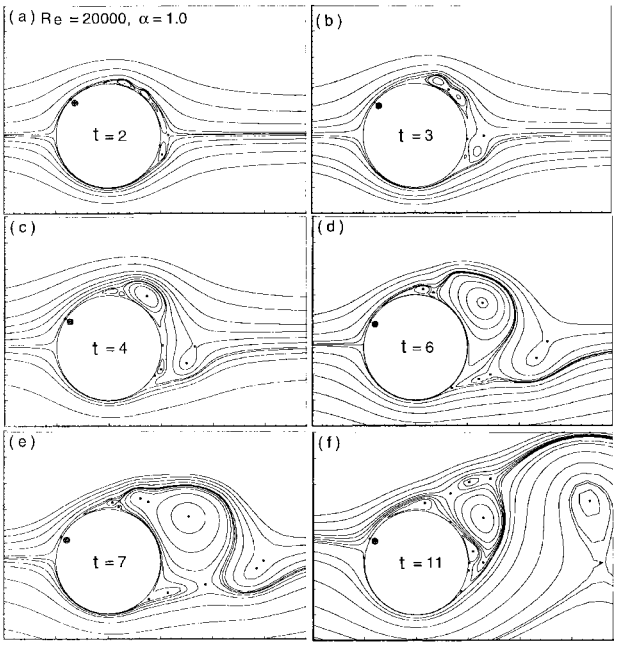

Figure 12. Near-wake flow pattern; (a)–(f) streamline plots.

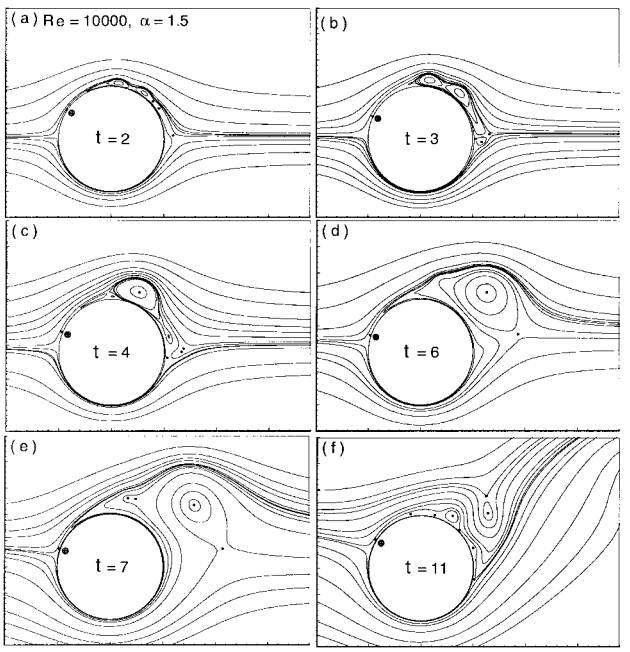

Figure 13. Near-wake flow pattern; (a)–(f) streamline plots.

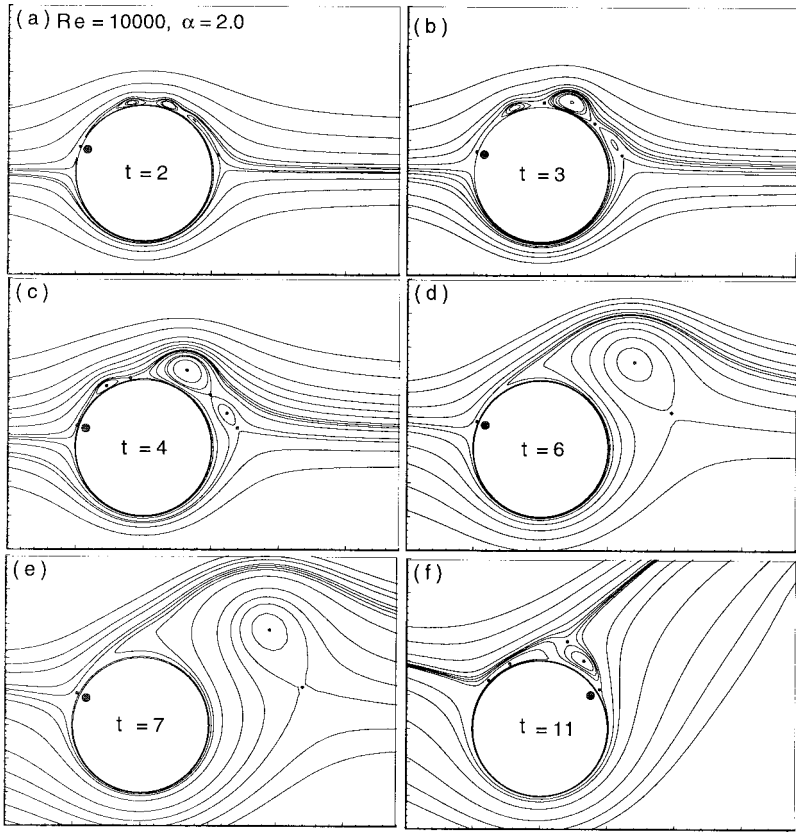

Figure 14. Near-wake flow pattern; (a)–(f) streamline plots.

between the closure points of E_1 and E_2 (if the latter exists), the initial developments are similar to those with $Re = 10^3$.

To reveal the large-time behavior, Figure 15(a–c) present the overall vorticity contours at $t = 20$ for $\alpha = 0.5$, 1 and 2 respectively. The corresponding time histories of the drag (C_D) and lift (C_L) coefficients are plotted in Figure 16(a,b). Note that the oscillation of C_L shifts, in general, from being of zero mean at $\alpha = 0$ to being of one sign as α increases. One exception is shown in Figure 17, and is related to high-Reynolds-number flow involving extra interaction between opposite main vortices as shown in Figures 10–12.

5. CONCLUSION

We have proposed a time-marching scheme to simulate unsteady two-dimensional flow past an impulsively started translating and rotating cylinder. In conjunction with the

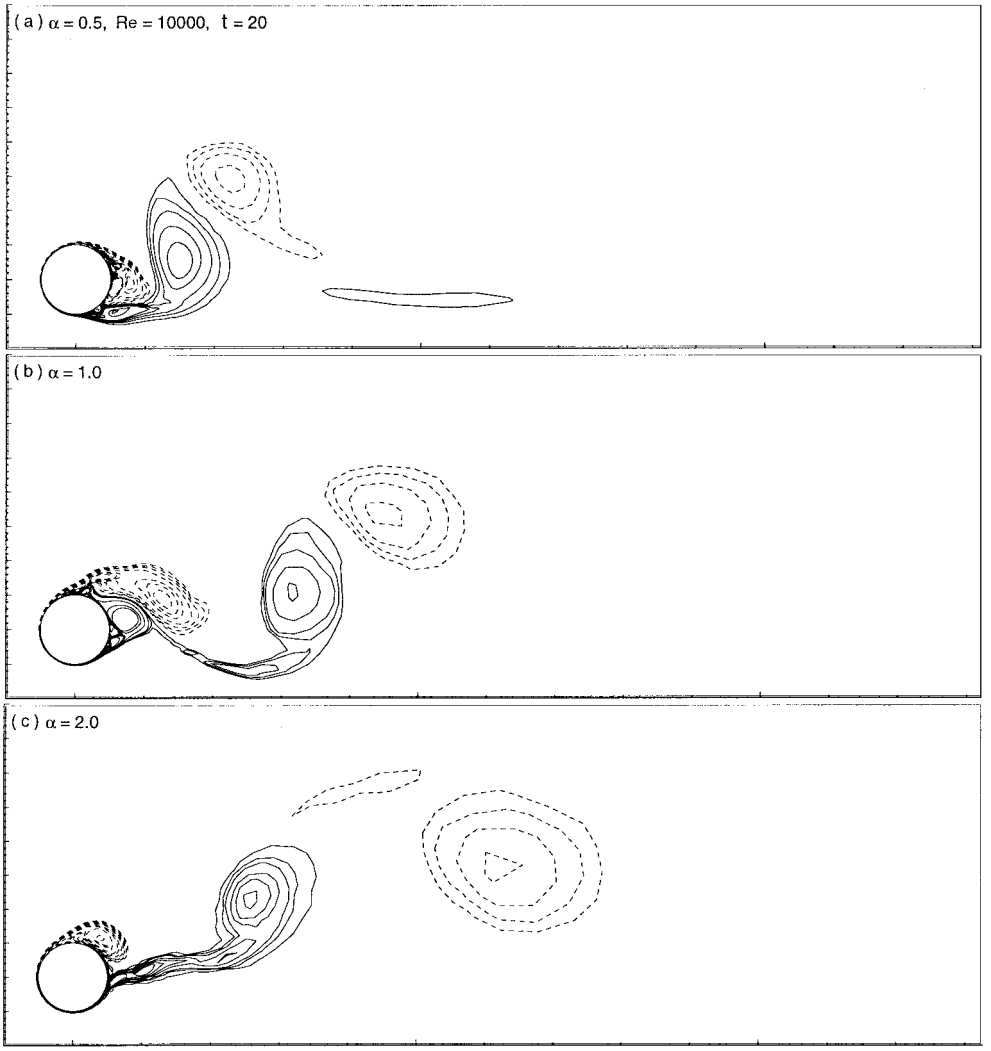

Figure 15. Overall vorticity contours (dash negative).

streamfunction–vorticity formulation of the Navier–Stokes equations, the wall vorticity, streamfunction, and interior vorticity are updated in turn and in an explicit manner for each time step. Up to moderately high Reynolds number and moderately high rotating speed, the numerical performance has been shown comparable with other more sophisticated methods.

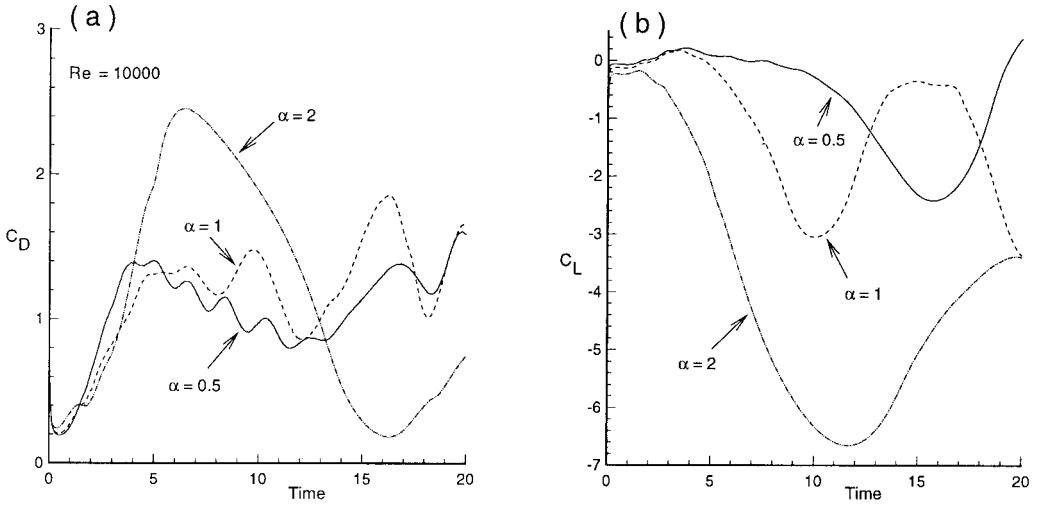

Figure 16. Time histories. (a) Drag coefficient; (b) lift coefficient.

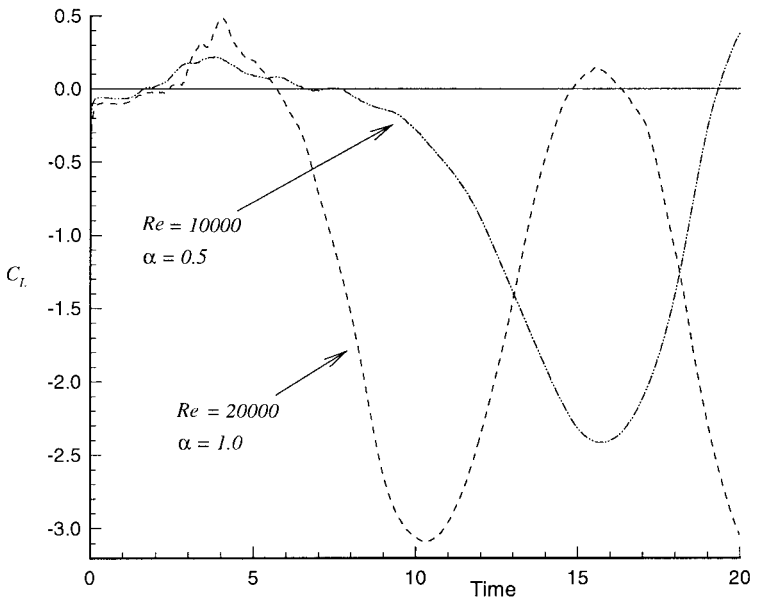

Figure 17. Time histories of lift coefficients.

ACKNOWLEDGMENTS

The author is grateful for the anonymous referees' comments. This research work was supported in part by the National Science Council under the grants NSC84-2112-M-001-052 and NSC87-2119-M-001-001.

REFERENCES

1. L. Prandtl and O. G. Tietjens, *Applied Hydro- and Aeromechanics*, Dover, New York, 1957.
2. G.K. Batchelor, *An Introduction to Fluid Dynamics*, Cambridge University Press, Cambridge, UK, 1967.
3. S. Taneda, 'Visual study of unsteady separated flows around bodies', *Prog. Aerospace Sci.*, **17**, 287–348 (1977).
4. R. Bouard and M. Coutanceau, 'The early stage of development of the wake behind an impulsively started cylinder for $40 < Re < 10^4$', *J. Fluid Mech.*, **101**(3), 583–607 (1980).
5. M. Coutanceau and C. Ménard, 'Influence of rotation on the near-wake development behind an impulsively started circular cylinder', *J. Fluid Mech.*, **158**, 399–446 (1985).
6. H.M. Badr and S.C.R. Dennis, 'Time-dependent viscous flow past an impulsively started rotating and translating circular cylinder', *J. Fluid Mech.*, **158**, 447–488 (1985).
7. Ta Phnoc Loc and R. Bouard, 'Numerical solution of the early stage of the unsteady viscous flow around a circular cylinder: a comparison with experimental visualization and measurements', *J. Fluid Mech.*, **160**, 93–117 (1985).
8. H.M. Badr, M. Coutanceau, S.C.R. Dennis and C. Ménard, 'Unsteady flow past a rotating circular cylinder at Reynolds numbers 10^3 and 10^4', *J. Fluid Mech.*, **220**, 459–484 (1990).
9. C.C. Chang and R.L. Chern, 'Vortex shedding from an impulsively started rotating and translating circular cylinder', *J. Fluid Mech.*, **233**, 265–298 (1991).
10. P.A. Smith and P.K. Stansby, 'Impulsively started flow around a circular cylinder by the vortex method', *J. Fluid Mech.*, **194**, 45–77 (1988).
11. M.H. Chou, 'An efficient scheme for unsteady flow past an object with boundary conformal to a circle', *SIAM J. Sci. Stat. Comput.*, **13**(4), 860–873 (1992).
12. M.H. Chou, 'Simulation of slightly viscous external flow by a grid-particle domain decomposition method', *Comput. Fluids*, **24**(3), 333–347 (1995).
13. M.H. Chou and W. Huang, 'Numerical study of high-Reynolds-number flow past a bluff object', *Int. J. Numer. Meth. Fluids*, **23**, 711–732 (1996).
14. A. Majda, J. McDonough and S. Osher, 'The Fourier method for non-smooth initial data', *Math. Comput.*, **32**, 1041–1081 (1978).
15. A. Harten, B. Engquist, S. Osher and S. R. Chakravarty, 'Uniformly high-order-accurate essentially non-oscillatory schemes III', *J. Comp. Phys.*, **71**, 231–303 (1987).
16. H. T. Huynh, 'Accurate monotone cubic interpolation', *SIAM J. Numer. Anal.*, **30**(1), 57–100 (1993).
17. C. W. Shu and S. Osher, 'Efficient implementation of essentially non-oscillatory shock capturing schemes', *J. Comp. Phys.*, **77**, 439–471 (1988).
18. M.H. Chou, 'Synchronization of vortex shedding from a cylinder under rotary oscillation', *Comput. Fluids*, **26**(8), 755–774 (1997).

